Wheel-rail impact at an insulated rail joint in an embedded rail system

Yang, Zhen; Zhang, Pan; Wang, Li

DOI
10.1016/j.engstruct.2021.113026

Publication date
2021

Document Version
Final published version

Published in
Engineering Structures

Engineering Structures 246 (2021) 113026

Contents lists available at ScienceDirect

Engineering Structures

journal homepage: www.elsevier.com/locate/engstruct

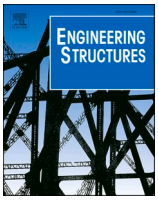

Wheel-rail impact at an insulated rail joint in an embedded rail system

Zhen Yang *, Pan Zhang, Li Wang

Delft University of Technology, Section of Railway Engineering, Stevinweg 1, 2628 CN Delft, the Netherlands

ARTICLE INFO

Keyword:
Finite element modelling
Embedded rail systems
Wheel-rail impact
Insulated rail joint
Hammer test
Pass-by measurement

ABSTRACT

With dynamic behaviour different from that of traditional discretely supported tracks, continuously supported embedded rail systems (ERSs) have been increasingly used in railway bridges, level crossings, trams, and high-speed lines. However, studies on ERSs have been limited, and none of them have addressed the wheel-rail impact-induced dynamic response, although wheel-rail impact is a main cause of ERS degradation. This paper studies, numerically and experimentally, the wheel-rail impact at an insulated rail joint (IRJ) used in the ERS. As a weak spot of the track, the IRJ results in discontinuities in the track support stiffness and wheel-rail contact geometry. This study first develops an explicit finite element model to simulate the vibration responses of the IRJ in the ERS when excited by a hammer and passing wheel loads. The simulated dynamic behaviours (represented by the hammer-excitation frequency response function) at a frequency up to 5 kHz and a wheel-rail impact vibration frequency up to 10 kHz are then validated with a field hammer test and a train pass-by measurement, respectively. Both the experimental study and numerical modelling reveals that the major frequencies of the impact vibration at the IRJ in the ERS depend mainly on geometric irregularities in the IRJ region and the train speed, rather than on the resonances of the track structure, as in the case of the discretely supported IRJ. This finding is meaningful to the engineering practice because it indicates a continuously supported IRJ in the ERS is more impact resistant, especially when the IRJ geometry is adequately maintained, e.g. by timely grinding.

1. Introduction

An embedded rail system (ERS) presents an innovative constraint mechanism for the rail by providing continuous elastic support [1–3]. In this system, the rail is enclosed and bonded by an elastic poured compound (EPC) in a steel or concrete groove (see Fig. 1). At the bottom of the groove, a resilient rubber strip is used to provide track elasticity and constrain the rail deflection in the vertical direction. Space-saving components such as PVC tubes may be included in the groove to conserve the EPC material and facilitate cable set-up. Compared with the traditional track supported by sleepers and ballasts, the ERS reduces the track height and weight and requires less maintenance work [4]. It also has the advantage of providing an obstacle-free surface with a lower construction height for crossing traffic. Owing to these advantages, the ERS has been increasingly used in railway bridges, level crossings, trams and high-speed lines since the 1970s [5–9]. It is, however, worth noting that when severe degradation occurs, e.g., cracks and debonding [10], the replacement cost of the ERS can be much higher than that of the traditional track.

Degradation of the ERS generally happens much faster at wheel-rail impact-exciting locations, typically insulated rail joints (IRJs), which are used for train positioning, signal transmission and control. However, to the best of our knowledge, none of the ERS studies [5–10] have addressed the ERS response induced by wheel-rail impact. The IRJ is a weak spot of the track structure because it introduces significant discontinuities in the geometry and stiffness. When a train passes an IRJ, large wheel-rail impact forces occur. These forces accelerate the degradation of the IRJ and adjacent track components and excite high-level impact vibration and noise, which is a nuisance to passengers and residents close to the railway lines.

Extensive studies have been conducted on IRJs to reduce track maintenance costs and environmental impacts [11–25]. Considering that the wheel-rail contact geometry is discontinuous at an IRJ, the traditional contact theories based on the non-conforming contact assumption, e.g., Hertzian contact theory [26] and Carter's theory [27], are no longer effective for the prediction of the contact stresses in the IRJ region [28,29]. Moreover, the wheel-IRJ impact vibration has high-frequency (up to 10 kHz) characteristics [23] and is difficult to accurately predict with multi-body dynamic models in which rails are treated as beams [30,31]. To address the aforementioned two issues, the explicit

* Corresponding author.
E-mail address: z.yang-1@tudelft.nl (Z. Yang).

https://doi.org/10.1016/j.engstruct.2021.113026
Received 14 September 2020; Received in revised form 27 July 2021; Accepted 13 August 2021
Available online 20 August 2021

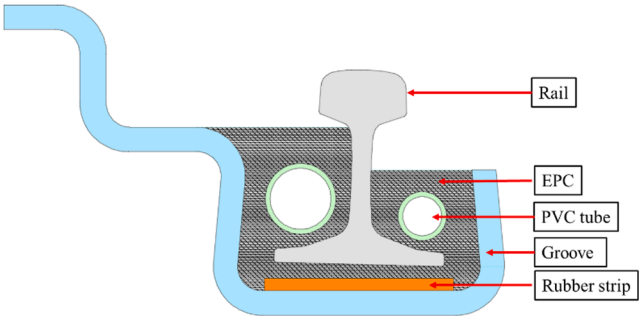

Fig. 1. The cross-section of the ERS.

finite element method (FEM), which can handle wheel-rail dynamic interactions with arbitrary contact geometry and high-frequency dynamic effects, has been widely employed in the study of wheel-IRJ impacts [12,16,22–25].

However, existing studies focus only on discretely supported IRJs, i.e., IRJs in traditional tracks supported by sleepers. This study investigates the wheel-rail impact at a continuously supported IRJ in the ERS, or EIRJ, for short. The crucial difference between the dynamic behaviour of the continuously supported EIRJ and the discretely supported IRJ in the traditional track causes different wheel-rail impact behaviours, i.e., the impact force and the consequent vibration and noise. This study thus investigates the wheel-EIRJ impact in two aspects: the dynamic behaviour of an EIRJ as the cause and the wheel-rail impact vibration at the EIRJ as the consequence.

By developing a 3D explicit finite element (FE) vehicle-EIRJ interaction model, this study simulates the vibration response of an EIRJ excited by a hammer and by a passing wheel. In the EIRJ model, the rail is supported 'continuously' by parallel spring-damper element pairs in three dimensions. A field hammer test is performed to calibrate the parameters of the spring-damper elements [32,33] and to ensure that the dynamic behaviour (represented by the hammer-excitation frequency response function (FRF)) of the target EIRJ up to 5 kHz is properly modelled. The simulated wheel-rail impact vibration up to 10 kHz is then validated with a train pass-by measurement at the target EIRJ. By comparing the dynamic behaviour and the impact vibration of the EIRJ to those of the discretely supported IRJ reported in [23], this study finds that the dominant frequencies of the impact vibration at the EIRJ depend mainly on the geometric irregularities in the IRJ region and on the train speed rather than on the resonances of the track structure, as in the case of the discretely supported IRJ.

2. Modelling of wheel-EIRJ interactions

2.1. Field conditions of the target EIRJ

An EIRJ on the Moerdijk bridge in the Netherlands is selected as the study target. The Moerdijk bridge is a 1026-m-long steel railway bridge that connects the mainline Rotterdam-Dordrecht of the Dutch railway network. The ERS is used on the bridge (see Fig. 2(a)) with unidirectional traffic and a maximum operating speed of 140 km/h. The cross-section of the ERS is shown in Fig. 1. The rail profile is UIC 54E1 with an inclination of 1/40. The EPC in the steel groove is Corkelast developed by the edilon)(sedra company. The Trackelast rubber strips are glued in the groove to mainly provide vertical track elasticity. The ERS on this bridge was renewed in July 2017, and the measurements involved in this study were conducted one year after renewal. Because the measured vibration responses of the four EIRJs at the same cross-section of the ERS showed similar dynamic characteristics, one of them, marked by the yellow frame in Fig. 2(a), was chosen as the target EIRJ and analysed in this paper. Fig. 2(b) depicts the close-up of the target EIRJ. Some wear, but no severe damage, was found on the joint and the adjacent track.

2.2. The FE vehicle-EIRJ interaction model

A 3D FE vehicle-EIRJ dynamic interaction model was developed, as shown in Fig. 3. A Cartesian coordinate system is adopted in the model, where the ×, y and z axes are oriented in the longitudinal (rolling), lateral and vertical directions, respectively. This model consists of three parts: a vehicle model, an EIRJ model and a wheel-rail contact model. The vehicle was modelled by a half-wheelset with the sprung mass of the car body and bogie supported by the primary suspension. The simplification of the vehicle without considering the secondary suspension is acceptable in the wheel-rail impact analysis because the vibration of the sprung mass on the secondary suspension has a negligible effect on the wheel-rail high-frequency dynamic interaction [34]. The wheel was modelled using 8-node solid elements, and the conicity of the wheel tread is 1/40, corresponding to that at the centre tread of a passenger car wheel of the Dutch railway with the standard profile of S1002.

The car body and bogie were modelled by eight mass elements connected to eight nodes on the central line of the wheel axle by vertical spring-damper pairs (for each, the stiffness = 1.15 MN/m and the damping = 2.5 kNs/m) serving as the primary suspension, as shown in Fig. 3. In the FE modelling, applying a load to discrete solid element nodes (in this case, the eight nodes on the central line of the wheel axle), rather than to a continuum as in real life, may cause unrealistic local deformations, even the error 'negative volume', i.e., the deformation is so significant that it exceeds the size of the element and the normal of the bounding face is towards the inside. How large the unrealistic deformation is induced depends mainly on the value of the load, the material

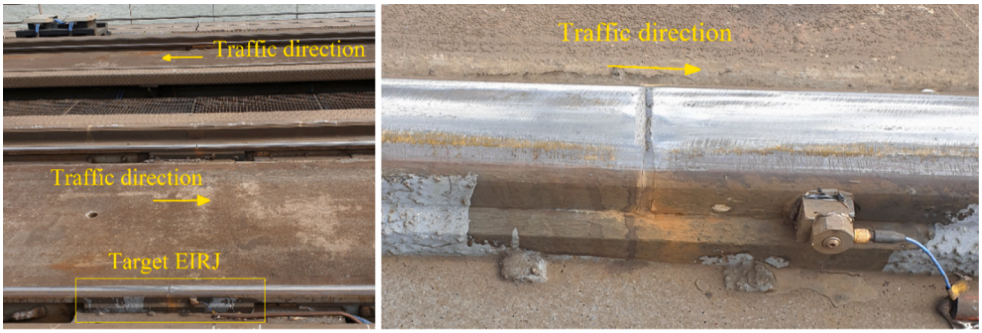

Fig. 2. The field condition of the target EIRJ. (a) An overview of the ERS on the Moerdijk bridge and the location of the target EIRJ; (b) A close-up of the target EIRJ. A 3D accelerometer was mounted on the field side of the rail head after the joint to measure train pass-by vibration.

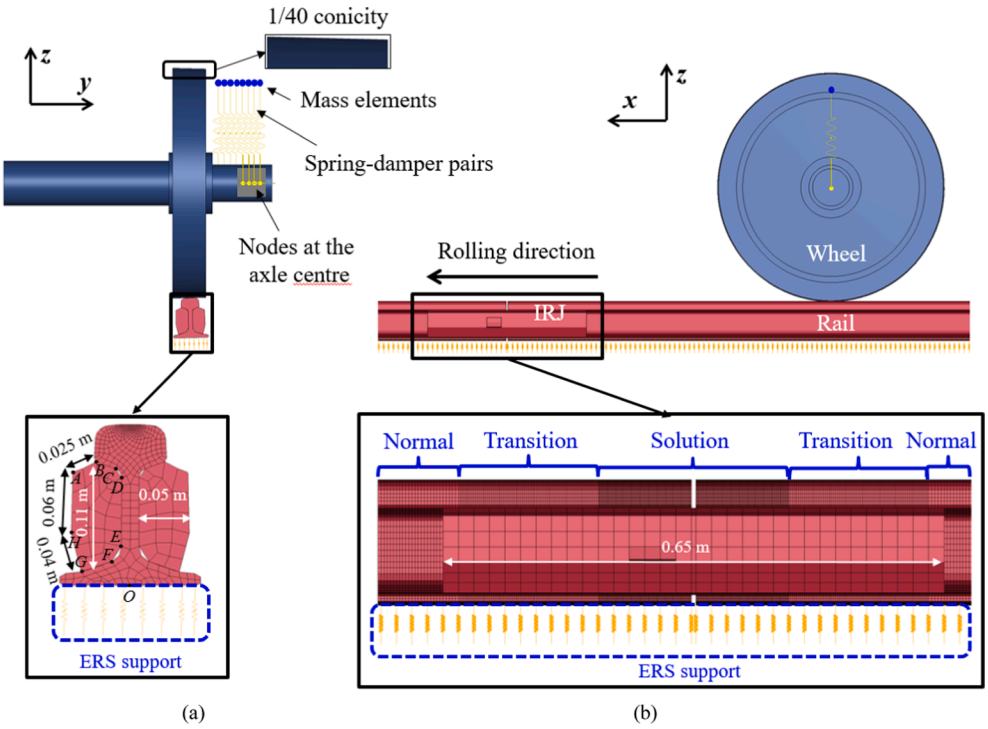

Fig. 3. The 3D FE vehicle-EIRJ dynamic interaction model. (a) Front view and a close-up of the track model. (b) Side view and a close-up of the EIRJ model. The ERS support was modelled with parallel spring-damper element pairs in the vertical, longitudinal and lateral directions. Non-uniform meshing was used: the element sizes in the wheel-rail contact solution zone, transition zones and normal zones were 1 mm, 5 mm and 10 mm, respectively. The measured rail geometry was adopted in the solution zone, and the nominal rail geometry was used in the transition and normal zones.

properties of the elements as well as the number of the element nodes subjected to the load. In the simulation of wheel-rail contact, the sprung mass (approximately 10 tons for the Dutch passenger trains) and the material properties (see the nominal values of steel in Table 1) are set. By distributing a load to more element nodes, the load applied to each node and the consequent unrealistic deformations of elements can be reduced. 'Negative volume' was observed when distributing the sprung mass to a small number (1 ~ 4 in this simulation case) of element nodes. This error can be reflected by a dramatic reduction of the computation time step, which is determined by the smallest element dimension to guarantee the stability of the explicit integration [35]. Extensive FE studies on the wheel-rail dynamic contact have shown that when the sprung mass is distributed to eight nodes, unrealistic local deformations have a negligible effect on the simulated wheel-rail contact solutions [24,34] and wheel/track structural dynamic responses [23,36,37]. Therefore, eight element nodes were used in this study to bear the load from the sprung mass. It can be expected that when the simulation results of interest rely heavily on the stress/strain of the elements where unrealistic deformations happen, e.g. cracking of the wheel axle, more element nodes are needed to further reduce the unrealistic deformations.

The distance from the wheel central plane to the closest spring-damper pair is 0.11 m, and the distance between each two adjacent spring-damper pairs is 0.024 m. The displacements of the mass elements were constrained in the lateral direction. In the rolling direction, the mass elements were coupled to each other, as well as to the connected nodes at the wheel axle centre (i.e. the mass elements and the connected nodes have the same motion). Symmetric boundary conditions were applied on the wheel axle to constrain the lateral movement.

Table 1
Values of the parameters used in the FE vehicle-EIRJ model.

Component	Parameter	Value
Rail, fishplate, wheel	Young's modulus	210 GPa
	Poisson's ratio	0.3
	Density	7850 kg/m^3
ERS support	Vertical stiffness	150 MN/m/m
	Vertical damping	45 kN·s/m
	Longitudinal stiffness	40 MN/m/m
	Longitudinal damping	105 kN·s/m
	Lateral stiffness	65 MN/m/m
	Lateral damping	80 kN·s/m

The ERS was modelled as a 10-m-long half-track with an IRJ in the middle. The IRJ is composed of two fishplates and a 6-mm-wide gap. The fishplates were modelled with their nominal geometry using 8-node solid elements and in an integrated mesh with the rails. The fishplates are symmetrical about the joint gap and their dimensions (height = 0.11 m, thickness = 0.05 m and length = 0.65 m) are denoted in the close-ups in Fig. 3. The point coordinates (y, z) of the fishplate cross-section in the yz-plane are given: A = (−0.054,0.113), B = (−0.031,0.123), C = (−0.012, 0.115), D = (−0.006, 0.107), E = (−0.008, 0.039), F = (−0.018, 0.024), G = (−0.048, 0.014), H = (−0.057, 0.053). The origin of the coordinate system O = (0,0) is at the centre of the rail bottom. The insulation layer between two rail ends was not modelled because of its much lower elastic modulus compared to the rails. This simplification has been proven to be appropriate for IRJ modelling [23,24]. The rail was modelled using 8-node solid elements, and the rail profile corresponds to the nominal UIC 54E1 profile. Non-uniform meshing was used for the rail to achieve accurate solutions with reasonable model size. The element sizes in the wheel-rail contact solution zone, transition zones and normal zones, indicated in Fig. 3(b), are 1 mm, 5 mm and 10 mm, respectively. The support of the ERS was modelled with parallel spring-damper element pairs in the vertical, longitudinal and lateral directions based on the experimental results (which will be shown later in Fig. 6) that only one pronounced resonance—rail mass on the vertical support stiffness of the ERS—is observed below 5 kHz. The longitudinal distance of each two adjacent spring-damper pairs is 10 mm. The top end of a spring-damper pair was connected to the rail node, and the bottom end was fixed. The stiffness and damping parameters were calibrated by the best fitting of the simulated FRFs to the measured results [32,33], as shown in detail in Section 3.3. The support stiffness was calibrated by fitting the simulated and measured resonance frequencies (positions of the FRF peaks), and the damping values were calibrated by fitting the sharpness of the FRF peaks. In this study, the parameters were fitted manually by trial and error with a step of 5 MN/m/m for stiffness and 5

kN·s/m for damping. The calibrated stiffness and damping parameters and the nominal material properties of the wheel, rails, and fishplates are listed in Table 1.

The wheel-rail contact model applied an automatic surface-to-surface contact scheme based on the penalty contact algorithm [35]. The rail surface was treated as the master surface, and the wheel surface was treated as the slave surface. The wheel-rail friction coefficient was 0.35 [34]. No geometric irregularities were applied to the wheel-rail contact surface except in the solution zone close to the gap of the rail model. The measured geometry of the target EIRJ (see Section 4.1) was adopted to reproduce a realistic wheel-rail contact.

An implicit-explicit sequential approach was employed in the simulation to minimise the solution time and the dynamic effects during the initialization of wheel-rail interaction [35]. In the implicit calculation, the vehicle-EIRJ system reached an equilibrium state under gravity. The calculated nodal displacement was subsequently inputted as an initial condition of the explicit calculation of the vehicle-EIRJ dynamic interaction. In the explicit calculation, initial forward translation and rotation velocities were prescribed to the wheel model to initiate rolling motion. The same initial translation velocity was applied to the car body and bogie. The wheel was subsequently driven by a torque (19 kN·m) applied on the axle to roll along the rail from the initial position towards the joint 1.326 m away, thus generating a wheel-rail traction force. The simulated wheel rolling distance is 1.625 m. The adopted integration time step was sufficiently small (79 ns) to ensure the stability of the integration and the contact [35].

The validation of the 3D FE vehicle-EIRJ model requires the validation of the three parts of the model. The dynamic behaviour of the wheel was validated by a modal analysis up to 5 kHz in [23]. The explicit FE wheel-rail contact model has been systematically verified with Hertz theory, Spence solution, Cattaneo solution and Kalker's CONTACT [34,38–43]. Therefore, the remaining task is to validate the dynamic behaviour of the newly developed EIRJ model.

3. Experimental study on the dynamic behaviour of the EIRJ

Hammer tests have been widely used to study the dynamic behaviour of track structures and to identify the in-service track parameters [44]. We performed hammer tests in this study not only to validate the FE EIRJ model but also to gain insights into the dynamic behaviour of the target EIRJ. The vertical and lateral FRFs of the EIRJ up to a frequency of 5 kHz were obtained, and the proposed EIRJ model was then calibrated and validated in the vertical and lateral directions. The longitudinal dynamic behaviour of the EIRJ was not measured because of the difficulty of applying longitudinal excitation to the rail head.

3.1. Hammer tests in the vertical direction

3.1.1. Set-up of the hammer test

Fig. 4 shows the set-up of the vertical hammer test. Six unidimensional accelerometers were used, denoted by S1–S6 in Fig. 4. They were placed on the rail top at three cross-sections before the joint and at symmetric cross-sections after the joint: close to (approximately 15 mm away from) the rail ends (S3 and S4), above the outer bolts of the fishplates (S2 and S5), and 0.6 m away from the joint (S1 and S6), where different vibration responses are expected. The diameter of the bolts is 45 mm, and the bolt positions can be found in Fig. 4.

The hammer excitations in the vertical direction were conducted as close as possible to accelerometers S3 and S4, as indicated by the red arrows in Fig. 4. At each hitting position, the excitations and responses of five impacts were recorded. Two types of hammers were used to excite the target EIRJ in a broad frequency range. A big hammer (PCB 086D50) with a softer tip was employed to provide low-frequency excitations, and a small hammer (PCB 086D05) with a harder tip was used to give high-frequency excitations. The upper limits of the valid frequency ranges (3 dB drop [44]) excited by the big and small hammers are 600 Hz and 5 kHz, respectively. Therefore, in the experimental results, the valid frequency range was between 100 Hz and 5 kHz. The lower frequency limit was 100 Hz because the big hammer might not be able to fully excite the steel bridge, which influences the dynamic behaviour of tracks at low frequencies [45]. The ambient temperature was approximately 15 °C.

3.1.2. Experimental results

After the synchronised acquisition of the acceleration and force signals, the FRF can be calculated by Eq. (1) [46]:

$$H_{ij}(f) = \frac{S_{a_i F_j}(f)}{S_{F_j F_j}(f)} \tag{1}$$

where $H_{ij}(f)$ is the FRF measured with the accelerometer Si (i = 1,2,3,4,5,6) when hitting the position close to the accelerometer Sj (j = 3,4); $S_{a_i F_j}$ is the cross-spectrum between the force F_j and the acceleration a_i, and $S_{F_j F_j}$ is the auto-spectrum of the force F_j. When the accelerometer i and the hitting position j are in the same location, $H_{ij}(f)$ is called direct accelerance; otherwise, it is called transfer accelerance.

Fig. 5 shows one example of the measured FRFs (H_{33}) excited by the big and small hammers. Above 1 kHz, the accelerance obtained with the big hammer fluctuates significantly and is much lower than that obtained by the small hammer, indicating that the big hammer cannot sufficiently excite rails above 1 kHz [44,45]. The accelerance excited by a small hammer is slightly larger than that excited by a big hammer at frequencies lower than 300 Hz, probably because the small hammer cannot fully excite the substructure, and thus, more excitation energy is absorbed by the rail. Therefore, the combination of the red FRF curve (obtained with the big hammer below 500 Hz) and the blue FRF curve (obtained with the small hammer between 500 Hz and 5 kHz) is considered the FRF of the target EIRJ.

The measured accelerances at the positions of accelerometers S1–S6 under vertical hammer excitation at position 3 are shown in Fig. 6. The vertical dynamic behaviour of the EIRJ can be analysed approximately in four frequency ranges: 100–400 Hz, 400 Hz–2 kHz, 2–4 kHz and 4–5 kHz, as divided by the red lines in Fig. 6. In the frequency range 100–400 Hz, the phases at these six positions are close to each other,

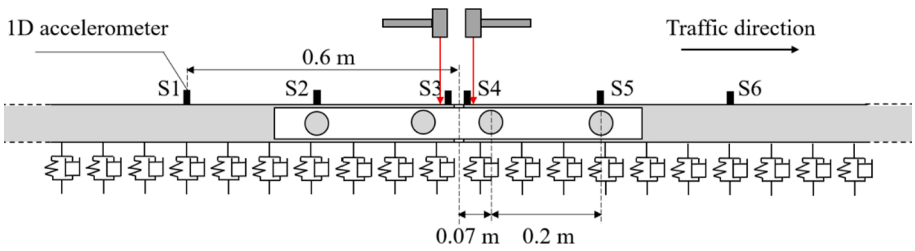

Fig. 4. The set-up of the hammer test in the vertical direction. Six 1D accelerometers were placed on the rail top and are denoted by S1–S6 along the traffic direction. S1 and S6 are 0.6 m away from the joint; S2 and S5 are above the outer bolts of the fishplates; S3 and S4 are close to the rail ends. The two red arrows indicate the hammer excitations in the vertical direction, conducted as close as possible to accelerometers S3 and S4.

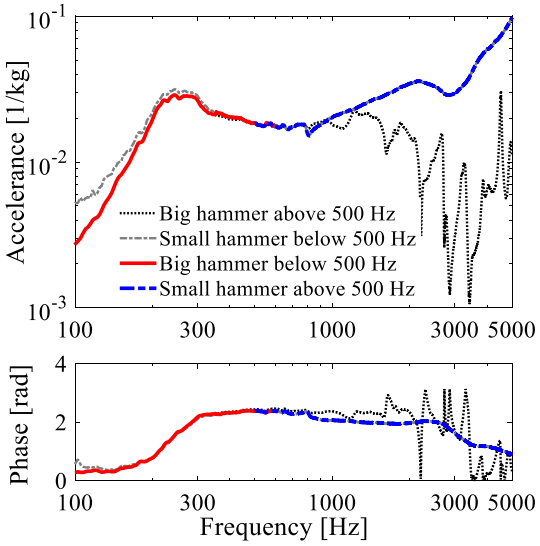

Fig. 5. A comparison of the accelerances of the EIRJ measured with the big and small hammers. The red curve obtained with the big hammer below 500 Hz and the blue curve obtained with the small hammer above 500 Hz constitute the FRF of the target EIRJ.

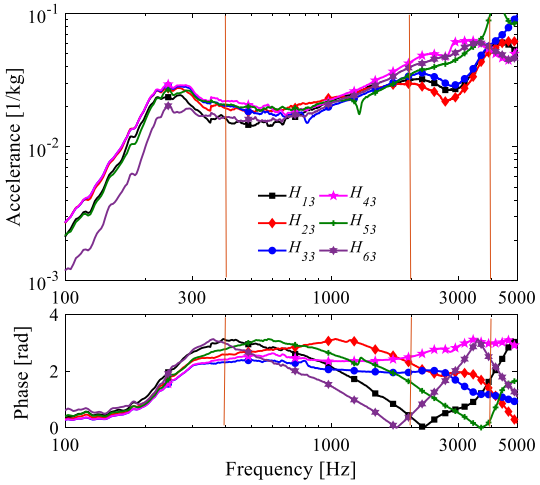

Fig. 6. A comparison of the measured accelerances with the six accelerometers S1–S6 under the vertical hammer excitations close to accelerometer S3. The legend H_{ij} denotes the FRF measured with the accelerometer *Si* (i = 1,2,3,4,5,6) when hitting the position close to the accelerometer *Sj* (j = 3,4).

indicating the in-phase movement of the whole ERS. The accelerance level decreases from the cross-section of the rail end where the excitation was conducted to positions away from the joint, which is caused by vibration energy decay during propagation. A dominant frequency at 260 Hz is observed by all the accelerometers, corresponding to a resonance of the rail mass on the vertical support stiffness of the ERS [44].

In the frequency range of 400 Hz–2 kHz, the accelerances at the six cross-sections along the rail almost overlap with each other, indicating that the rail vibration decays insignificantly in this frequency range. The phase lags at these six positions show a remarkable difference with increasing frequencies, which suggests different propagation velocities of vibration at various frequencies. This is because the vertical vibrational waves in the rail are dispersive [47], and thus, the phase velocities change at various frequencies.

In the frequency range of 2–4 kHz, the accelerances of the ERS before the joint (H_{13} H_{23} H_{33}) have similar tendencies, which are, however, greatly different from those after the joint (H_{43} H_{53} H_{63}). The peak of accelerances H_{13} H_{23} H_{33} at approximately 2100 Hz and a dip at approximately 2800 Hz are not observed in the accelerances H_{43} H_{53} H_{63}. We can thus conclude that this difference is caused by the existence of the IRJ, which leads to a support stiffness discontinuity of the ERS. In the frequency range of 4–5 kHz, the direct accelerance H_{33} is larger than the transfer accelerances at positions 1, 2, 4, and 6, which could be caused by the rapid decay of near-field waves at position 3. Accelerance H_{53} has a conspicuous resonance peak at approximately 4100 Hz, possibly due to a local defect at position 5.

Fig. 7 compares the direct and transfer accelerances at positions 3 and 4. The good agreement of the direct accelerances H_{33} and H_{44} indicates a good symmetry of the ERS with respect to the IRJ. This also suggests that the track support degradation of the target EIRJ from the wheel-rail impact is still insignificant. The good agreement of the transfer accelerances H_{34} and H_{43} indicates that reciprocity can be observed at the target EIRJ.

3.2. Hammer tests in the lateral direction

3.2.1. Set-up of the hammer test

Fig. 8 shows the top-view set-up of the hammer tests in the lateral direction. A 3D accelerometer (see also Fig. 2(b)) was mounted on the field side of the rail head 80 mm away after the EIRJ. The lateral hammer excitations were conducted on the gauge face of the rail close to the joint at the same cross-sections as the vertical ones, denoted by the two red arrows in Fig. 8. Only the small hammer was used for the lateral excitations because of the limited hitting areas on the rail gauge face.

3.2.2. Test results

Fig. 9 shows the lateral accelerances excited at positions 3 and 4 and measured by the 3D accelerometer (shown in Fig. 8). Below 500 Hz, the lateral accelerances and phases in these two cases basically overlap with each other, indicating in-phase movement on both sides of the EIRJ. The lateral rail resonance, which occurs at approximately 120 Hz, is less pronounced than the vertical resonance. In the frequency range of 500–2600 Hz, the accelerance by the excitation at position 3 is larger than that at position 4, and at higher frequencies, the opposite tendency is found. With these two adjacent excitation positions before and after the EIRJ, this difference should be related to the support stiffness discontinuity of the ERS at the IRJ. Comparing Fig. 9 with Fig. 6, it is found that the general accelerance level of the EIRJ in the lateral direction is higher than that in the vertical direction.

3.3. Calibration and validation of the EIRJ model

To calibrate the vertical stiffness and damping of the ERS, the vertical accelerances simulated with the EIRJ model are fitted to the measured results at the six positions, as shown in Fig. 10. The excitation was performed vertically at position 3. As depicted in Fig. 10, good agreement between the simulation and the measurement is achieved at all six positions up to 5 kHz, which indicates that the proposed model is capable of accurately simulating the high-frequency dynamics behaviour of the EIRJ. The rail resonance at 260 Hz was well reproduced in the simulation by the calibrated parameters of the vertical stiffness and damping listed in Table 1. The differences between the accelerances before the EIRJ (H_{13} H_{23} H_{33}) and after the EIRJ (H_{43} H_{53} H_{63}) in the frequency range of 2–4 kHz were also identified in the simulation. These results indicate that the EIRJ model can accurately simulate vibration transmission from one rail to the other. The conspicuous resonance peak at approximately 4100 Hz in H_{53} was not found in the simulation. One possible reason is that some local defects happen at position 5, leading to a local resonance. It is worth noting that oscillations are observed in the simulated accelerances in the frequency range of 600 Hz–3 kHz, whereas the measured curves are relatively smooth. These phenomena have been reported in [23], and are considered to be related to the finite track model length.

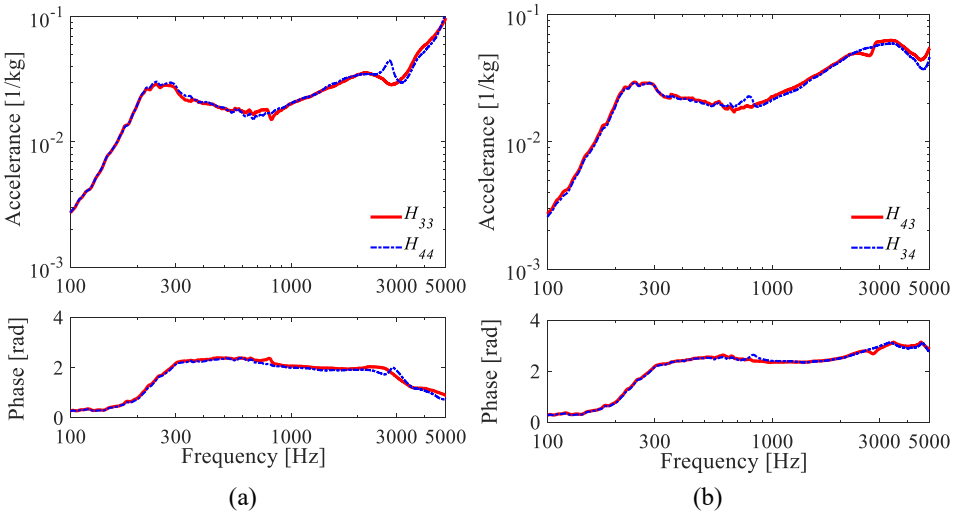

Fig. 7. Comparisons of the measured accelerances with accelerometers S3 and S4 under vertical excitations close to each of them. H_{ij} denotes the FRF measured with the accelerometer S*i* (i = 3,4) when hitting the position close to the accelerometer S*j* (j = 3,4). (a) Comparison of the direct accelerances measured with accelerometers S3 (H_{33}) and S4 (H_{44}). (b) Comparison of the transfer accelerances H_{43} and H_{34}.

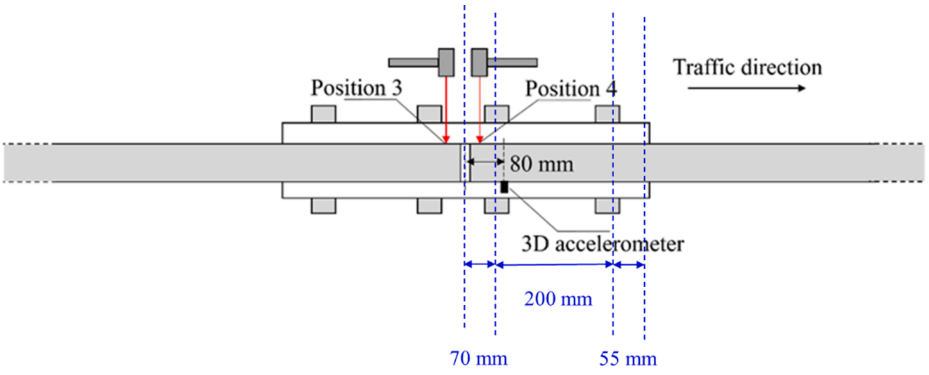

Fig. 8. Top view of the set-up for the hammer test in the lateral direction. A 3D accelerometer was placed on the field side of the rail head 80 mm away after the joint. The hammer excitations were conducted in the lateral direction at the same cross-sections as the vertical hammer tests (the cross-sections are close to the 1D accelerometers S3 and S4, denoted by Position 3 and Position 4).

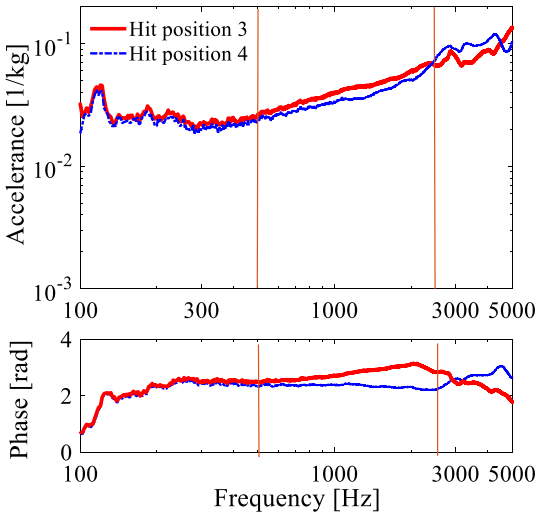

Fig. 9. Comparison of the lateral accelerances measured with the 3D accelerometer under hammer excitations at Positions 3 and 4.

The closest fits of the simulated to the measured lateral accelerances by the lateral excitation at positions 3 and 4 are shown in Fig. 11. Reasonable agreement between the simulation and the measurement is achieved up to 5 kHz. The lateral rail resonance at approximately 120 Hz is reproduced in the simulation, but the peaks are less sharp than the measurement results. The difference in the accelerances above 500 Hz between the two excitation positions is also reproduced, which is caused by the support stiffness discontinuity at the EIRJ. The oscillations in the simulated lateral accelerances and phase in the frequency range of 500 Hz–2 kHz have also been found in the simulated accelerances of the traditional discretely supported IRJ [23]. This could be caused by the finite track model length as in the vertical direction accelerances and/or the simplification of the lateral ERS support, which does not include a lateral constraint of the rail web in the model.

3.4. Discussion

In this section, the proposed EIRJ model was calibrated and validated by a field hammer test. The model was proven to be capable of simulating the high-frequency dynamic behaviour of the EIRJ in the vertical and lateral directions. A rail resonance was found at 260 Hz in the vertical direction and at 120 Hz in the lateral direction. Compared to the traditional track, the 1st and 2nd pinned–pinned resonances [23,48] in the vertical and lateral directions are avoided by the continuous

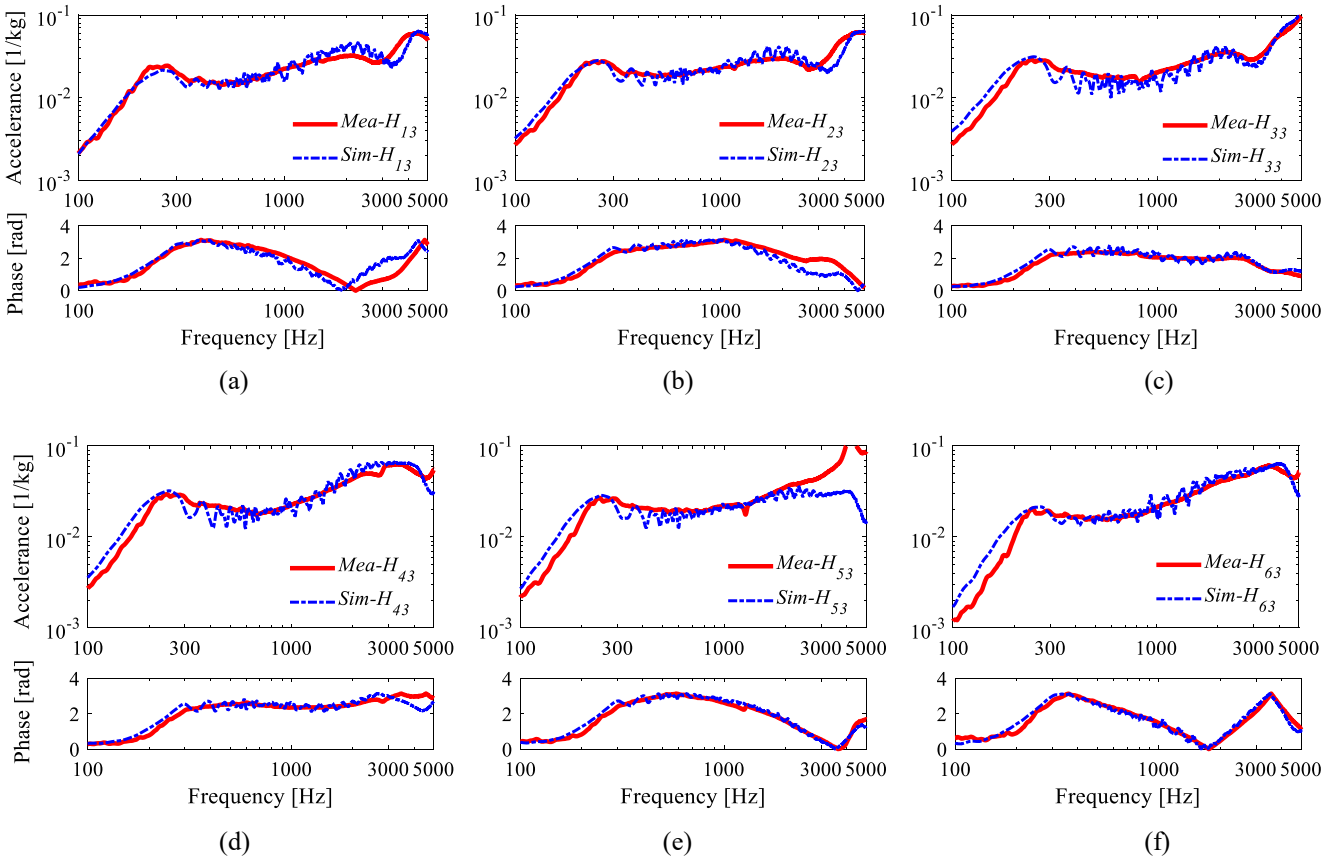

Fig. 10. Comparisons of the simulated and measured accelerances at the positions of accelerometers S1–S6 under vertical hammer excitations close to accelerometer S3. H_{i3} ($i = 1,2,3,4,5,6$) denotes the FRF measured with accelerometer Si when hitting the position close to accelerometer S3. (a) H_{13}; (b) H_{23}; (c) H_{33}; (d) H_{43}; (e) H_{53}; and (f) H_{63}.

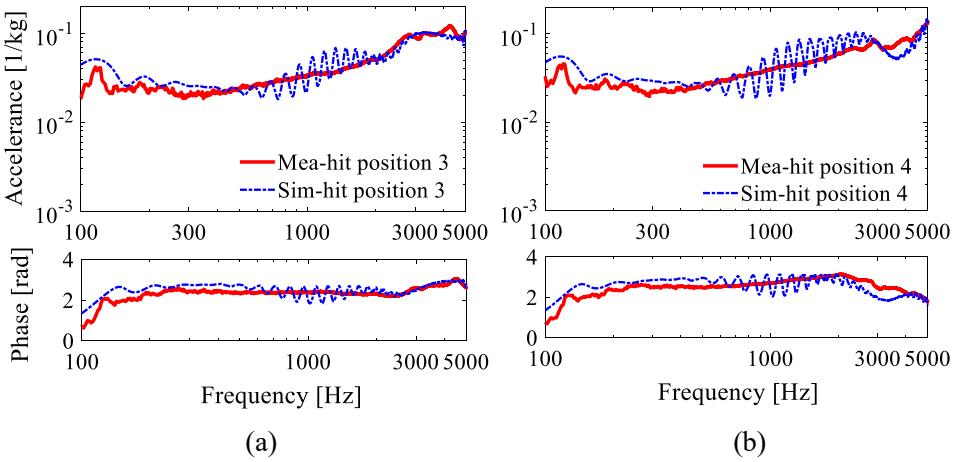

Fig. 11. Comparison of the simulated (Sim-) and measured (Mea-) lateral accelerances at the position of the 3D accelerometer. (a) Under the hammer excitations at position 3. (b) Under the hammer excitations at position 4.

support of the ERS. Therefore, the ERS may potentially mitigate the corrugation [49] and noise [23,47] induced by the pinned–pinned resonances.

The dynamic parameters of the ERS support in the vertical and lateral directions were derived by fitting the simulations to field hammer test results. The longitudinal parameters were calibrated by fitting the simulated wheel-rail impact vibration to the measurement results in Section 4.2. The obtained vertical and longitudinal dynamic stiffnesses in this paper are approximately 1.5 times larger than the measured static stiffness at 15 °C [8]. The reason is that the stiffness of the viscous material in the ERS, including the Corkelast (EPC) and rubber strips, is frequency-dependent, in which the stiffness increases for higher frequencies [8]. In our case, the derived stiffness reflects the dynamic behaviour of the ERS up to 5 kHz and thus corresponds to a larger value than the static behaviour reported in [8]. This also suggests that using frequency-dependent parameters in the simulation instead of constant parameters may achieve a closer fit to the measurements, which could be further analysed in future research.

4. Simulation and measurements of wheel-IRJ impact vibration at the ERS

In this section, we employ the vehicle-EIRJ interaction model to simulate wheel-rail impact vibration at an IRJ supported by ERS. In this simulation, a rail profile of the EIRJ measured with a 3D scanner is used to represent the real wheel-rail contact geometry. The simulated vibration responses are then validated by a train pass-by measurement.

4.1. EIRJ geometry measurement

The surface geometry of the target EIRJ is measured with a laser-based 3D scanner (HandyScan) and then used in the vehicle-EIRJ interaction model. In the measurement, the laser strips project a reference on the rail surface, which is captured by two cameras. The precision of the HandyScan is 30 μm in arbitrary directions. Fig. 12(a) shows the measured 3D geometry. The longitudinal-vertical profiles extracted from the rail top surface along the five yellow lines in Fig. 12(a) are compared in Fig. 12(b). Line 1 is 7 mm away from the gauge side, and the distance between two adjacent yellow lines is 8 mm. Line 2 is approximately in the middle of the running band because of the asymmetric running band on the rail surface, as shown in Fig. 2(b). Fig. 12(c) and (d) show the nominal (without wear and deformation) and measured geometries of the EIRJ, respectively. The measured geometry is used in the FE simulations. The measured profile of the EIRJ has a major dip with a length of approximately 70 mm, as shown in Fig. 12(b). This geometric discontinuity is caused by wear and plastic deformation at the rail ends due to train passages. The maximum depth of the dip is 0.25 mm on Line 2. In addition, a smaller dip is found on the running band (at the position of Lines 1–3) of the rail just after the joint.

4.2. Comparison of the simulated and measured impact vibrations

A pass-by measurement with a train speed of 130 km/h was conducted on the target EIRJ on the 22nd of June 2018. The vertical, longitudinal and lateral impact vibrations were measured by the 3D accelerometer shown in Fig. 8. The sampling frequency is 25.6 kHz.

The pass-by measurement was numerically reproduced by the proposed FE vehicle-EIRJ interaction model using the implicit-explicit sequential approach mentioned in Section 2.2. Fig. 13, Fig. 14 and Fig. 15 compare the measured and simulated wheel-rail impact vibrations in the vertical, longitudinal and lateral directions, respectively. Each figure includes the time-history accelerations, the corresponding power spectrum densities (PSDs) and wavelet power spectra (WPSs). The average time-history accelerations and PSDs of four wheel passages are provided to reduce the random errors caused by the wheel profile, hunting motion and suspension. Fig. 13 shows that the simulated vertical impact vibration agrees excellently with the pass-by measurement in both the time and frequency domains. Fig. 13(b) and (c) indicate that the vertical vibration energy is mainly concentrated at two major frequencies of approximately 550 Hz and 7 kHz. The impact vibration with a major frequency of 550 Hz has a duration of approximately 10 ms, which is much longer than that of the rapidly decaying signal at 7 kHz, as indicated by the white rectangles a and b in Fig. 13(c).

According to the measured EIRJ geometry and train speed, the two major frequencies of 550 Hz and 7 kHz are believed to be excited by the 70-mm-long dip and the 6-mm-wide gap of the EIRJ based on the formula shown in Eq. (2):

$$f = \frac{v}{L} \tag{2}$$

where f is the vibration frequency excited by the rail irregularity, v is the

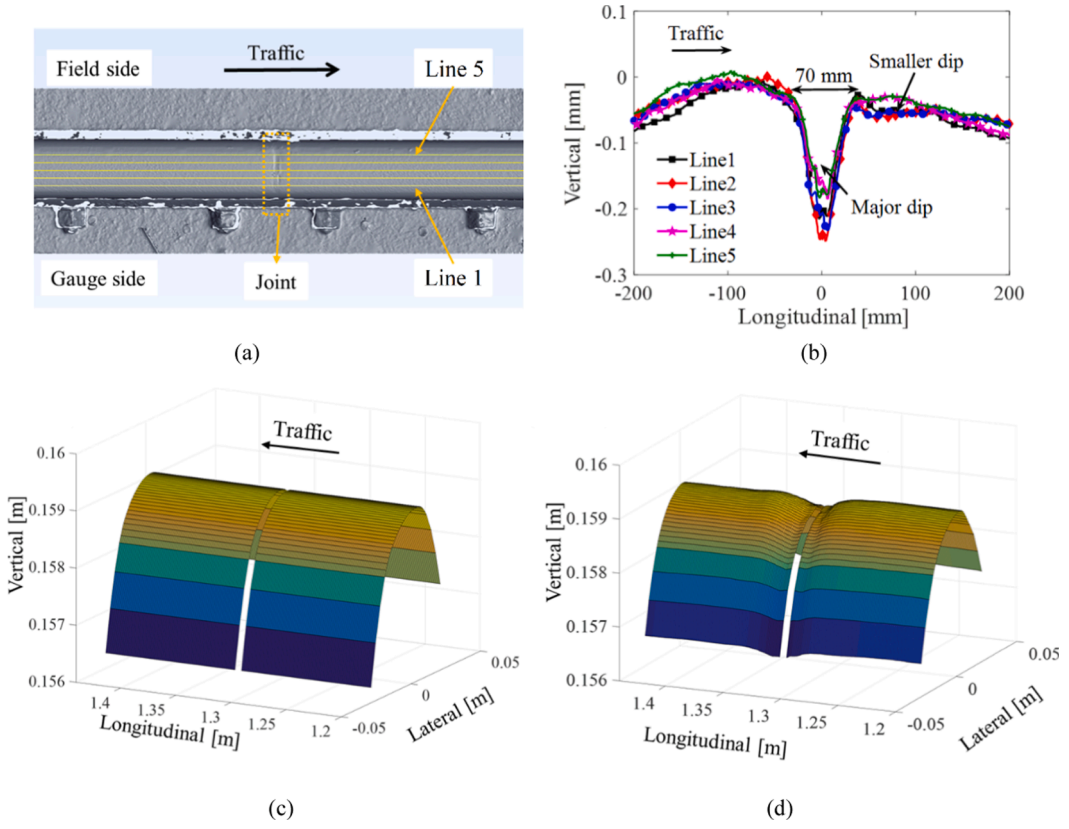

Fig. 12. The rail geometry at the target EIRJ. (a) The 3D EIRJ geometry measured with a 3D scanner; the five yellow lines Line 1 ~ Line 5 on the rail top indicate the cross-sections where the 2D geometries were extracted and compared. (b) The five measured 2D longitudinal-vertical rail profiles extracted on the rail top surface. (c) The nominal EIRJ geometry without wear and plastic deformation. (d) The measured EIRJ geometry used in the FE simulations.

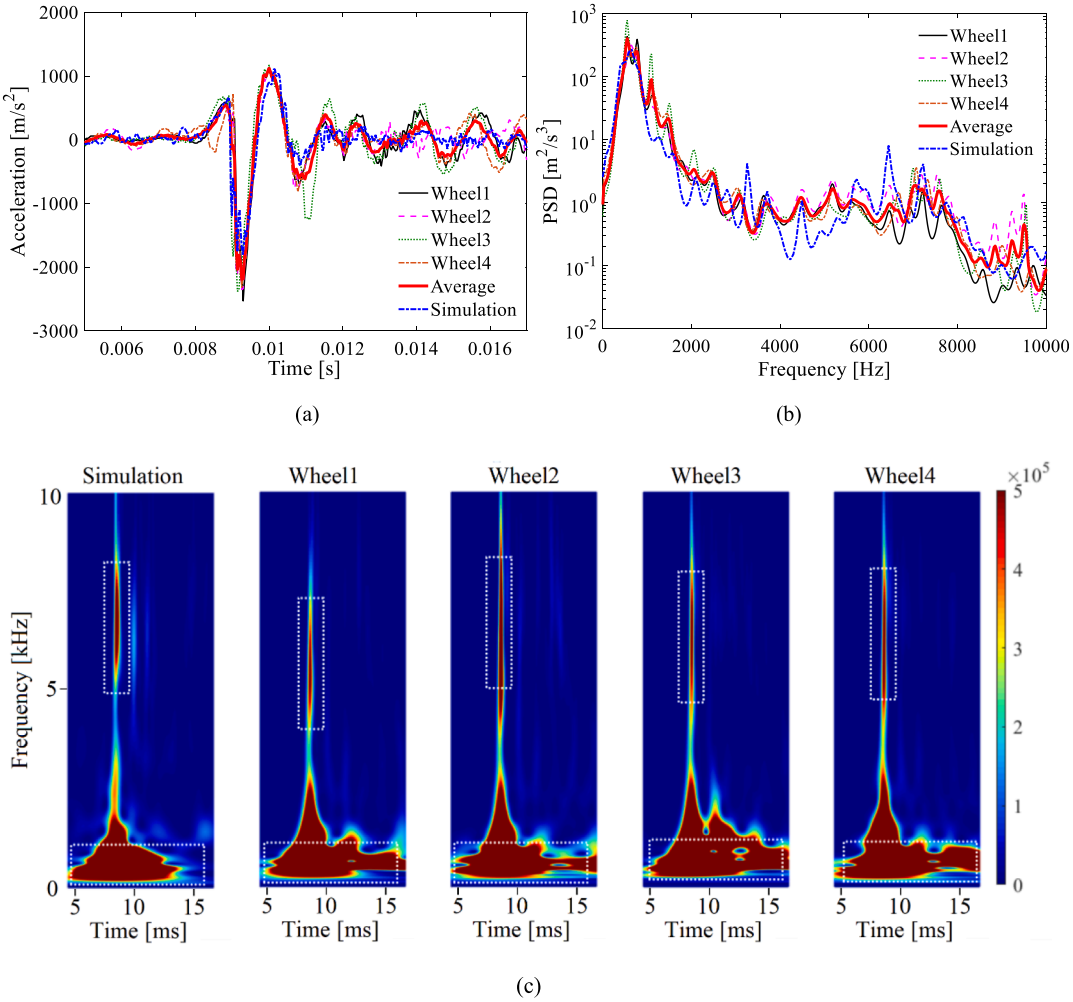

Fig. 13. Comparison of the simulated and measured vertical wheel-rail impact vibrations. The curve 'Average' plots the average of the measured impact vibration induced by the four passing wheels of one coach. (a) Time-history signals; (b) PSDs; and (c) WPSs. (The white dashed boxes indicate the dominant frequency components of the signals).

train speed and L is the irregularity wavelength. The rail resonance frequency at approximately 260 Hz is not observed in the measured and simulated impact vibration signals. In other words, the major frequencies of impact vibration at the EIRJ depend mainly on the wheel-rail contact geometry and train speed, rather than on the resonance frequencies of the IRJ reported in [23] for the case of a traditional discretely supported IRJ. A slight difference between the simulation and measurement is found in Fig. 13(a) and Fig. 13(c), where the simulated results underestimate the vibration responses after 0.013 s in the frequency range of 400–800 Hz. This may be caused by the larger vertical damping of the ERS support in the simulation, which is derived by fitting the simulated vertical accelerance to the hammer test measurement.

Agreement between the simulation and the measurement is achieved in the longitudinal direction in terms of the acceleration amplitude, major frequency components, and wavelet power, as shown in Fig. 14. The major frequencies of the longitudinal impact vibration are at approximately 550 Hz and 7 kHz, the same as those in the vertical direction, which should also be excited by the dip and gap of the EIRJ. However, compared to the vertical direction, in which the wheel-rail interaction mainly acts, the impact vibration energy at 550 Hz is significantly smaller. The simulation overestimates the longitudinal vibration signals in the frequency range of 400 Hz–1 kHz, as shown by the white dashed frame in Fig. 14(c). In this frequency range, the track support plays an important role in the track vibration [47]; thus, the difference between the simulation and the measurement may be caused by the simplification of the ERS support in the model.

The simulated and measured impact responses in the lateral direction are depicted in Fig. 15. Overall, reasonable agreement is achieved in terms of the major frequency components of approximately 550 Hz and 7 kHz. Compared to that in the vertical and longitudinal directions, the vibration energy in the lateral direction is considerably smaller, indicating a weak wheel-IRJ impact interaction. Therefore, the lateral vibration responses are more easily influenced by the randomness of the traffic, such as wheel profiles, hunting motions and suspension conditions. This can be seen from the relatively poor repeatability of the four measurement results. These random traffic factors cannot be considered in the simulation, leading to difficulty in obtaining a good match between the simulation and measurement.

5. Discussion

The dynamic behaviour and the wheel-rail impact response of the proposed 3D FE vehicle-EIRJ interaction model were validated against a field hammer test and a train pass-by measurement, respectively. The model was further employed to analyse the reduction of vibration and noise (the main advantage of ERS) as well as the formation mechanism of EIRJ profile degradation (e.g., wear, plastic deformation) caused by wheel-rail impacts. To study the material cracking and debonding in the ERS, which are typical degradation types of ERS, a more complex model with detailed modelling of the ERS components (i.e., the EPC, rubber

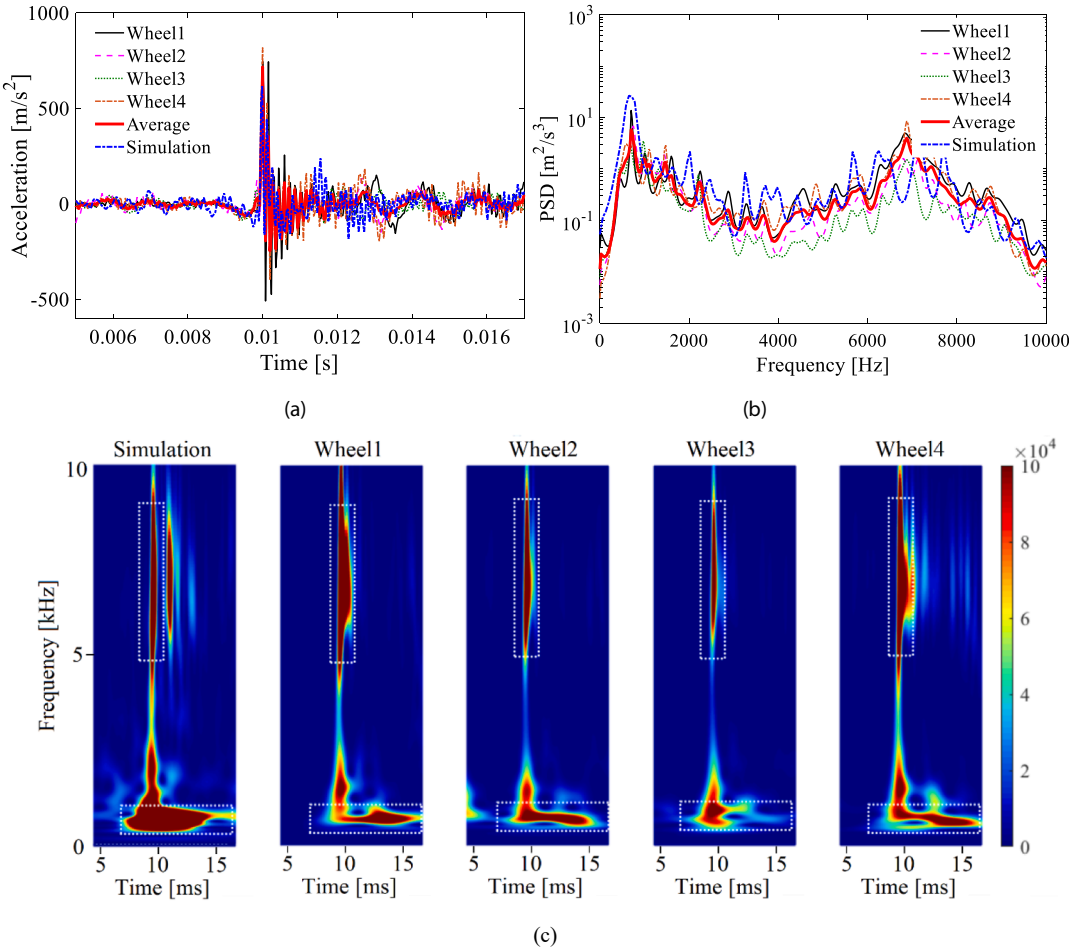

Fig. 14. Comparison of the simulated and measured longitudinal wheel-rail impact vibrations. The curve 'Average' plots the average of the measured impact vibration induced by the four passing wheels from one coach. (a) Time-history signals; (b) PSDs; and (c) WPSs. (The white dashed boxes indicate the dominant frequency components of the signals).

strip, PVC tubes and steel groove) was built up, which has, however, not been validated against field measurements because of the complexity of the material properties and interfaces of the ERS components. In future work, the test set-up reported in [33] can be applied to determine the frequency- and temperature-dependent material properties of EPCs and rubber strips. The treatment of the interfaces of the ERS components, either by defining the contact or applying constraints, can then be calibrated by hammer tests. Since the nonlinear material properties of the polymer-based components and the nonlinear track support stiffness can be fully considered, the detailed model is expected to provide more accurate dynamic behaviour and impact responses of the ERS than other models.

6. Conclusions and future work

This paper studied, numerically and experimentally, the wheel-rail impact at an IRJ supported by an ERS, i.e., an EIRJ. A 3D explicit FE vehicle-EIRJ dynamic interaction model was developed. The continuous support of the ERS was modelled by parallel spring-damper element pairs based on the hammer test. The result showed that only one pronounced resonance—the rail mass on the vertical support stiffness of the ERS—was observed below 5 kHz. The EIRJ model was calibrated and validated by a field hammer test in the vertical and lateral directions. Good agreement between the simulated and measured hammer-excitation frequency response functions indicated that the proposed model is capable of accurately simulating the high-frequency dynamic behaviour of the target EIRJ up to 5 kHz. The simulated wheel-EIRJ impact vibration was then validated by a train pass-by measurement at the target EIRJ, and agreement up to 10 kHz was achieved between the simulation and measurement. The major findings are summarised as follows.

- The vertical dynamic behaviour of the EIRJ was characterised in four frequency ranges: 100–400 Hz, 400 Hz–2 kHz, 2–4 kHz and 4–5 kHz. The whole ERS vibrates vertically in phase at 100–400 Hz; the rail vibration decays less significantly at 400 Hz–2 kHz in the EIRJ region; the discontinuity of the support stiffness of the ERS at the IRJ may cause significantly different vibration responses of the rails before and after the joint at 2–4 kHz; and rapid decay of near-field waves is observed at 4–5 kHz.
- The lateral dynamic behaviour of the EIRJ was characterised in three frequency ranges: 100–500 Hz, 500–2600 Hz, and 2600 Hz–5 kHz. The whole ERS vibrates laterally in phase at 100–500 Hz. The vibration level of the rail before the joint is higher than that after the joint at 500–2600 Hz but lower at 2600 Hz–5 kHz. This difference is probably related to the support stiffness discontinuity of the ERS at the IRJ.
- Compared to the traditional discretely supported track, the continuously supported ERS does not have the 1st and 2nd pinned–pinned resonances in the vertical and lateral directions and can thus avoid the related track defects, vibration and noise.
- The wheel-rail impact vibration at the IRJ supported by the ERS has two major frequencies at approximately 550 Hz and 7 kHz, which are

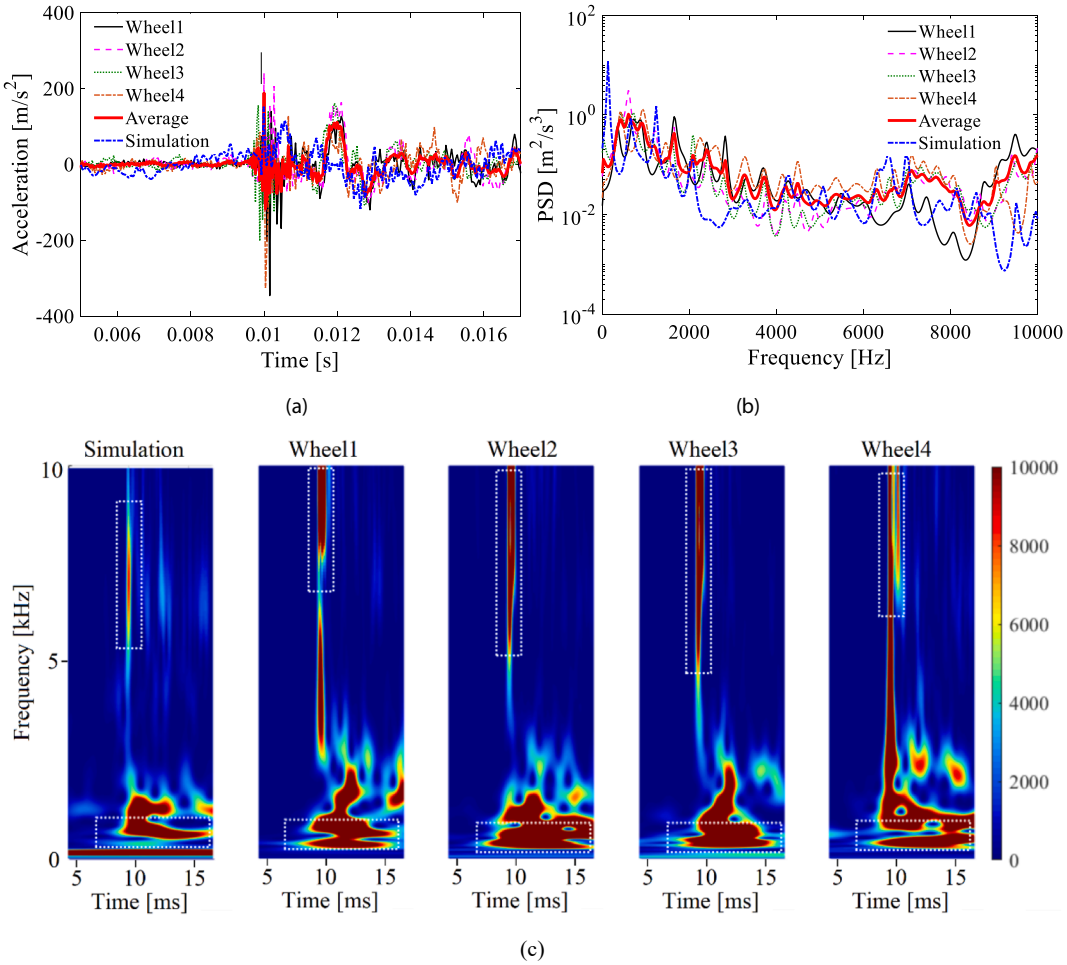

Fig. 15. Comparison of the simulated and measured lateral wheel-rail impact vibrations. The curve 'Average' plots the average of the measured impact vibration induced by the four passing wheels from one coach. (a) Time-history signals; (b) PSDs; and (c) WPSs. (The white dashed boxes indicate the dominant frequency components of the signals).

excited by the 70-mm-length dip and the 6-mm-width gap, respectively, of the EIRJ with a train speed of 130 km/h.

- The major frequencies of the impact vibration at the continuously supported EIRJ depend mainly on the geometric irregularities in the EIRJ region and on the train speed, rather than the resonance frequencies of the track structure, as is the case of the discretely supported IRJ. The EIRJ can thus be more impact resistant, especially when the joint geometry is adequately maintained, e.g., by timely grinding.

A 0.25-mm-deep major dip and a 0.02-mm-deep smaller dip due to degradation were observed in the measured EIRJ geometry (see Fig. 12 (b)). The EIRJ profile degradation is caused by the large wheel-rail impact force at the EIRJ. Since the explicit FE wheel-rail interaction model is suitable for calculating the wear and plastic deformation of the rail surface, the vehicle-EIRJ interaction model developed in this study can be further used to analyse the formation mechanism of these defects and propose countermeasures. By fitting the simulated accelerances of the EIRJ model to the hammer test results, this work also derived the ERS support parameters (i.e., stiffness and damping) in the service condition. The derived ERS support parameters can be used as indicators for the long-term monitoring of EIRJs in future work.

Declaration of Competing Interest

The authors declare that they have no known competing financial interests or personal relationships that could have appeared to influence the work reported in this paper.

References

[1] Ludvigh E. Elastic behaviour of continuously embedded rail systems. Periodica Polytechnica Civil Eng 2002;46:103–14.
[2] Kormos G. Longitudinal behaviour of rail embedded in elastic material. Periodica Polytechnica Civil Eng 2002;46:115–24.
[3] Major Z. Longitudinal behaviour of embedded rails. Acta Technica Jaurinensis 2015;8:179–87. https://doi.org/10.14513/actatechjaur.v8.n2.367.
[4] Edilon)(sedra, Complete Manual Embedded rail systems on bridges. https://www.edilonsedra.com/wp-content/uploads/2017/05/Complete-Manual-Embedded-Rail-Systems-on-Bridges.pdf [accessed 20.08.22] in.
[5] Ryjáček P, Howlader MM, Vokáč M, Stollenwerk B, Ondovčák P. The rail-bridge interaction – recent advances with ERS fastening system for steel bridges. Transp Res Procedia 2016;14:3972–81. https://doi.org/10.1016/j.trpro.2016.05.494.
[6] Ling L, Han J, Xiao X, Jin X. Dynamic behavior of an embedded rail track coupled with a tram vehicle. J Vib Control 2017;23(14):2355–72. https://doi.org/10.1177/1077546315616521.
[7] Zhao Y, Li X, Lv Q, Jiao H, Xiao X, Jin X. Measuring, modelling and optimising an embedded rail track. Appl Acoust 2017;116:70–81. https://doi.org/10.1016/j.apacoust.2016.07.021.
[8] Stančík V, Ryjáček P, Vokáč M. Thermal and load rate-dependent interaction between embedded rail system and bridge. Proc Inst Mech Eng, Part F: J Rail Rapid Transit 2019;233(3):326–36. https://doi.org/10.1177/0954409718795092.
[9] Markine VL, Man APd, Jovanovic S, Esveld C. Optimum design of embedded rail structure for high speed lines. In: international conference on railway engineering, Engineering Technics Press, Edinburgh, United Kingdom; 2000.
[10] Wang L, Wang P, Chen R, Li S, Li Z. Experimental and numerical investigation of damage development in embedded rail system under longitudinal force. Eng Fail Anal 2020;114:104590. https://doi.org/10.1016/j.engfailanal.2020.104590.

[11] Kerr AD, Cox JE. Analysis and tests of bonded insulated rail joints subjected to vertical wheel loads. Int J Mech Sci 1999;41:1253–72. https://doi.org/10.1016/S0020-7403(98)00042-3.
[12] Mandal NK, Dhanasekar M, Sun YQ. Impact forces at dipped rail joints. P I Mech Eng F-J Rai 2016;230(1):271–82. https://doi.org/10.1177/0954409714537816.
[13] Wu TX, Thompson DJ. On the impact noise generation due to a wheel passing over rail joints. J Sound Vib 2003;267(3):485–96. https://doi.org/10.1016/S0022-460X(03)00709-0.
[14] Himebaugh AK, Plaut RH, Dillard DA. Finite element analysis of bonded insulated rail joints. Int J Adhes Adhes 2008;28(3):142–50. https://doi.org/10.1016/j.ijadhadh.2007.09.003.
[15] Kabo E, Nielsen JCO, Ekberg A. Prediction of dynamic train-track interaction and subsequent material deterioration in the presence of insulated rail joints. Veh Syst Dyn 2006;44(sup1):718–29. https://doi.org/10.1080/00423110600885715.
[16] Cai W, Wen Z, Jin X, Zhai W. Dynamic stress analysis of rail joint with height difference defect using finite element method. Eng Fail Anal 2007;14(8):1488–99. https://doi.org/10.1016/j.engfailanal.2007.01.007.
[17] Mandal NK, Lewis R, Wen Z. Quantification of sub-surface railhead material damage due to composite endpost materials of insulated rail joints for cyclic wheel loadings. Eng Fail Anal 2020;113:104562. https://doi.org/10.1016/j.engfailanal.2020.104562.
[18] Fischer S, Major Z, Németh A. FEM modelling possibilities of glued insulated rail joints for CWR tracks. Acta Technica Jaurinensis 2020;13:42–84. https://doi.org/10.14513/actatechjaur.v13.n1.535.
[19] Samantaray SK, Mittal SK, Mahapatra P, Kumar S. Assessing the flexion behavior of bolted rail joints using finite element analysis. Eng Fail Anal 2019;104:1002–13. https://doi.org/10.1016/j.engfailanal.2019.06.057.
[20] Yang Zhen, Li Zili. A numerical study on waves induced by wheel-rail contact. Int J Mech Sci 2019;161-162:105069. https://doi.org/10.1016/j.ijmecsci.2019.105069.
[21] Molodova M, Oregui M, Núñez A, Li Z, Dollevoet R. Health condition monitoring of insulated joints based on axle box acceleration measurements. Eng Struct 2016;123:225–35. https://doi.org/10.1016/j.engstruct.2016.05.018.
[22] Wen Z, Jin X, Zhang W. Contact-impact stress analysis of rail joint region using the dynamic finite element method. Wear 2005;258(7-8):1301–9. https://doi.org/10.1016/j.wear.2004.03.040.
[23] Yang Z, Boogaard A, Chen R, Dollevoet R, Li Z. Numerical and experimental study of wheel-rail impact vibration and noise generated at an insulated rail joint. Int J Impact Eng 2018;113:29–39. https://doi.org/10.1016/j.ijimpeng.2017.11.008.
[24] Yang Z, Boogaard A, Wei Z, Liu J, Dollevoet R, Li Z. Numerical study of wheel-rail impact contact solutions at an insulated rail joint. Int J Mech Sci 2018;138–139:310–22. https://doi.org/10.1016/j.ijmecsci.2018.02.025.
[25] Zong N, Dhanasekar M. Experimental studies on the performance of rail joints with modified wheel/railhead contact. P I Mech Eng F-J Rai 2014;228(8):857–77. https://doi.org/10.1177/0954409713496764.
[26] Hertz H. Ueber die Berührung fester elastischer Körper. Journal für die reine und angewandte Mathematik (Crelle's J) 1882;1882. https://doi.org/10.1515/crll.1882.92.156.
[27] Carter FW. On the action of a locomotive driving wheel. P R Soc Lond a-Conta 1926;112:151–7. https://doi.org/10.1098/rspa.1926.0100.
[28] Chen YC, Kuang JH. Contact stress variations near the insulated rail joints. Proc Inst Mech Eng Part F: J Rail Rapid Transit 2002;216(4):265–73. https://doi.org/10.1243/095440902321029217.
[29] Chen Y-C, Chen L-W. Effects of insulated rail joint on the wheel/rail contact stresses under the condition of partial slip. Wear 2006;260(11-12):1267–73. https://doi.org/10.1016/j.wear.2005.08.005.
[30] Zhai W, SUN X. A detailed model for investigating vertical interaction between railway vehicle and track. Veh Syst Dyn 1994;23(sup1):603–15. https://doi.org/10.1080/00423119308969544.
[31] Zhai W, Cai Z. Dynamic interaction between a lumped mass vehicle and a discretely supported continuous rail track. Comput Struct 1997;63(5):987–97. https://doi.org/10.1016/S0045-7949(96)00401-4.
[32] Oregui M, Li Z, Dollevoet R. An investigation into the vertical dynamics of tracks with monoblock sleepers with a 3D finite-element model. P I Mech Eng F-J Rai 2016;230(3):891–908. https://doi.org/10.1177/0954409715569558.
[33] Oregui M, Li Z, Dollevoet R. An investigation into the modeling of railway fastening. Int J Mech Sci 2015;92:1–11. https://doi.org/10.1016/j.ijmecsci.2014.11.019.
[34] Zhao X, Li Z. The solution of frictional wheel-rail rolling contact with a 3D transient finite element model: validation and error analysis. Wear 2011;271(1-2):444–52. https://doi.org/10.1016/j.wear.2010.10.007.
[35] Yang Z, Deng X, Li Z. Numerical modeling of dynamic frictional rolling contact with an explicit finite element method. Tribol Int 2019;129:214–31. https://doi.org/10.1016/j.triboint.2018.08.028.
[36] Molodova M, Li ZL, Núñez A, Dollevoet R. Validation of a finite element model for axle box acceleration at squats in the high frequency range. Comput Struct 2014;141:84–93. https://doi.org/10.1016/j.compstruc.2014.05.005.
[37] Wei Z, Shen C, Li Z, Dollevoet R. Wheel-rail impact at crossings: relating dynamic frictional contact to degradation. J Comput Nonlinear Dyn 2017;12:041016. https://doi.org/10.1115/1.4035823.
[38] Kalker JJ. Three-dimensional elastic bodies in rolling contact. 1st ed. Netherlands: Springer; 1990.
[39] Yang Z, Li Z. Numerical modeling of wheel-rail squeal-exciting contact. Int J Mech Sci 2019;153–154:490–9. https://doi.org/10.1016/j.ijmecsci.2019.02.012.
[40] Wei Z, Li Z, Qian Z, Chen R, Dollevoet R. 3D FE modelling and validation of frictional contact with partial slip in compression-shift-rolling evolution. Int J Rail Transp 2016;4(1):20–36. https://doi.org/10.1080/23248378.2015.1094753.
[41] Deng X, Qian Z, Li Z, Dollevoet R. Applicability of half-space-based methods to non-conforming elastic normal contact problems. Int J Mech Sci 2017;126:229–34. https://doi.org/10.1016/j.ijmecsci.2017.04.002.
[42] Vo KD, Tieu AK, Zhu HT, Kosasih PB. A 3D dynamic model to investigate wheel–rail contact under high and low adhesion. Int J Mech Sci 2014;85:63–75. https://doi.org/10.1016/j.ijmecsci.2014.05.007.
[43] Ma Y, Markine V, Mashal AA, Ren M. Modelling verification and influence of operational patterns on tribological behaviour of wheel-rail interaction. Tribol Int 2017;114:264–81. https://doi.org/10.1016/j.triboint.2017.04.038.
[44] A.P. De Man, Dynatrack: A survey of dynamic railway track properties and their quality, doctoral thesis, TU Delft; 2002.
[45] Oregui M, Molodova M, Núñez A, Dollevoet R, Li Z. Experimental investigation into the condition of insulated rail joints by impact excitation. Exp Mech 2015;55(9):1597–612. https://doi.org/10.1007/s11340-015-0048-7.
[46] Maia N, Silva J. Theoretical and experimental modal analysis. England: Research Studies Press LTD; 1998.
[47] Thompson DJ. Wheel-rail noise generation, Part III: Rail vibration. J Sound Vib 1993;161(3):421–46. https://doi.org/10.1006/jsvi.1993.1084.
[48] Oregui M, Li Z, Dollevoet R. Identification of characteristic frequencies of damaged railway tracks using field hammer test measurements. Mech Syst Signal Pr 2015;54–55:224–42. https://doi.org/10.1016/j.ymssp.2014.08.024.
[49] Knothe K, Groß-Thebing A. Short wavelength rail corrugation and non-steady-state contact mechanics. Veh Syst Dyn 2008;46(1-2):49–66. https://doi.org/10.1080/00423110701590180.